INORGANIC CHEMISTRY
FRONTIERS

RESEARCH ARTICLE

View Article Online
View Journal | View Issue

Cite this: *Inorg. Chem. Front.*, 2025, **12**, 5506

An air-stable high-performance single-molecule magnet operating as a luminescent thermometer below its blocking temperature†

Julio Corredoira-Vázquez, [a,b,c] Cristina González-Barreira, [a] Matilde Fondo, *[a] Ana M. García-Deibe, [a] Jesús Sanmartín-Matalobos, [a,b] Silvia Gómez-Coca, [d] Eliseo Ruiz, [d] Carlos D. S. Brites [c] and Luís D. Carlos *[c]

Received 9th May 2025,
Accepted 3rd June 2025

DOI: 10.1039/d5qi01113b

rsc.li/frontiers-inorganic

The field of molecule magnets has advanced significantly in recent years. Yet, key challenges persist for their practical applications, such as achieving higher blocking temperatures and maintaining precise temperature control in air-stable magnets. This work addresses aspects related to both challenges. Thus, it presents the air-stable hexagonal bipyramidal compound $\{[Dy(L^{N6en})(OSiPh_3)_2](BPh_4)\}\cdot 1.5CH_2Cl_2$ ($\mathbf{1}\cdot 1.5CH_2Cl_2$) and its diluted analogue $\{[Dy_{0.1}Y_{0.9}(L^{N6en})(OSiPh_3)_2](BPh_4)\}\cdot 1.5CH_2Cl_2$ ($\mathbf{1@Y}\cdot 1.5CH_2Cl_2$). Their high axiality, achieved by reducing equatorial charge, enables magnetic behaviour with energy barriers higher than 1500 K and blocking temperatures based on hysteresis (T_B^H) of 12 and 40 K, respectively. Hence, $\mathbf{1@Y}\cdot 1.5CH_2Cl_2$ is the SMM with the highest T_B^H reported among air-stable uncapsulated molecule magnets. Besides, both complexes show temperature-dependent luminescence. Remarkably, $\mathbf{1@Y}\cdot 1.5CH_2Cl_2$ stands out as the pioneering example of a bifunctional molecule magnet and luminescent thermometer with both functionalities active below its T_B^H. This breakthrough makes it possible to monitor the temperature of a molecule in the range where it exhibits remanent magnetization for the first time. Moreover, this molecular material presents by far the best magnetic characteristics (U_{eff} and T_B^H) of any SMM luminescent thermometer reported to date. Experimental magnetic and luminescent data are analysed using theoretical calculations. Notably, luminescence is interpreted *via* coupled cluster methods, offering a more sophisticated alternative to the traditional time-dependent DFT approach.

Introduction

Multifunctionality is the future goal of new smart materials. In this context, the development of magneto-luminescent molecular materials is a scientific field of growing interest. Single molecule magnets (SMMs) are very promising due to its potential applications in technologically significant areas such as magnetic storage[1] and quantum computing.[2,3] However, one of the primary challenges to overcome before such technological applications become feasible is attaining their precise temperature control, which is essential for maintaining the magnetized state and preserving magnetic memory. Nevertheless, conventional thermometers are not suitable for measuring temperature at the nanoscale. Therefore, constructing microdevices based on SMMs with integrated thermometric capabilities could overcome this limitation. In this regard, obtaining SMMs with temperature-dependent luminescence represents a key issue.[4,5] Achieving this end will allow SMMs to function as *in situ* thermometers, enabling continuous self-monitoring of their temperature, thus avoiding the loss of magnetic behaviour resulting from excessive heating. Since the first compounds displaying dual SMM and luminescent thermometer characteristics, described in 2019,[6–9] the number of additional compounds with such bifunctional nature reported to date remains relative low.[10–29] Since then, there have been substantial enhancements in the magnetic and thermometric properties of these molecular nanomaterials. Accordingly, a few compounds have been described that show thermometric character in part of the temperature

---

[a] *Departamento de Química Inorgánica, Facultade de Química, Universidade de Santiago de Compostela, 15782 Santiago de Compostela, Spain. E-mail: matilde.fondo@usc.es*
[b] *Institute of Materials (iMATUS), Universidade de Santiago de Compostela, 15782 Santiago de Compostela, Spain*
[c] *Phantom-g, CICECO – Aveiro Institute of Materials, Physics Department University of Aveiro, 3810-193 Aveiro, Portugal. E-mail: lcarlos@ua.pt*
[d] *Departament de Química Inorgànica i Orgànica and Institut de Recerca de Química Teòrica i Computacional, Universitat de Barcelona, Diagonal 645, 08028 Barcelona, Spain*

† Electronic supplementary information (ESI) available. CCDC 2262113. For ESI and crystallographic data in CIF or other electronic format see DOI: **https://doi.org/10.1039/d5qi01113b**

range where they present slow relaxation of magnetization in the absence of an external field.[7,14–16,21–23] However, it is worth noting that none of these complexes behaves as a luminescent thermometer below the blocking temperature of the SMM.

Consequently, another major challenge in this research field is the obtaining of air-stable SMMs of high blocking temperature. In this regard, it should be noted that the blocking temperature based on magnetic hysteresis (T_B^H) of 80 K, established with an organometallic mononuclear SMM,[30] has not been surpassed, but matched with another dinuclear mixed valent dysprosium metallocene.[31] Nevertheless, the air instability of these organometallic compounds is challenging for their practical utility. This inconvenience has led to an active search for air-stable SMMs with improved properties. In this way, a dysprosium azafullerene with a 100-seconds blocking temperature of 45 K (T_B^H = 39 K) was recently reported,[32] but the current record of T_B^H for unencapsulated SMMs is 36 K, which is held by a dysprosium complex with pentagonal bipyramid geometry.[33] In recent years, other air-stable mononuclear SMMs with hexagonal bipyramid geometry have been obtained, with energy barriers exceeding 2400 K,[34] and blocking temperatures up to 20 K.[35] However, within SMMs that in turn behave as luminescent thermometers, the energy barriers and blocking temperatures do not exceed 944 K and 8 K, respectively.[23]

Developing lanthanoid luminescent thermometers with exceptionally high-energy barriers, leading to substantial crystal field (CF) splitting of both ground and excited state multiplets, presents a significant challenge. This arises because the thermal sensitivity of Boltzmann-type luminescent thermometers hinges on the energy gap between the thermally coupled excited states. Large energy gaps can compromise high relative thermal sensitivity across the entire temperature range where slow relaxation occurs.[36] Consequently, a fundamental obstacle remains in the development of molecular magnets that function as luminescent thermometers within their operational regime.

One potential way to circumvent this theoretical limitation would be to base the luminescent thermometric behaviour of the magnet not on the metal, but on the ligand. This would involve designing lanthanoid complexes with luminescent ligands that in turn predetermine a suitable geometry to favour high anisotropy. This strategy could lead to the improvement of the parameters U_{eff} and T_B^H in SMMs with luminescence thermometry, as well as to the achievement of the performance of both mentioned magnetic and optical properties in the same temperature range.

Building on these assumptions, we analyse the thermometric properties of the high-performance SMM $\{[\text{Dy}(\text{L}^{\text{N6en}})(\text{OSiPh}_3)_2](\text{BPh}_4)\}\cdot1.5\text{CH}_2\text{Cl}_2$ (**1**·$1.5\text{CH}_2\text{Cl}_2$). This analysis is based on ligand triplet emission coupled with Dy^{3+} luminescence. In addition, we also present here the bifunctional analogue $\{[\text{Dy}_{0.1}\text{Y}_{0.9}(\text{L}^{\text{N6en}})(\text{OSiPh}_3)_2](\text{BPh}_4)\}\cdot1.5\text{CH}_2\text{Cl}_2$ (**1@Y**·$1.5\text{CH}_2\text{Cl}_2$), which exhibits Dy^{3+}-based slow relaxation of the magnetization and ligand-based luminescence thermometry. Both compounds are molecule magnets that function as optical thermometers, with magnetic properties surpassing those of any SMM with luminescence thermometry described so far. Notably, **1@Y**·$1.5\text{CH}_2\text{Cl}_2$ is the first SMM capable of operating as a luminescent thermometer below its blocking temperature. Thus, **1@Y**·$1.5\text{CH}_2\text{Cl}_2$ shows bifunctionality up to 40 K.

Results and discussion, experimental

Synthesis and structural characterization

$\{[\text{Dy}(\text{L}^{\text{N6en}})(\text{OSiPh}_3)_2](\text{BPh}_4)\}\cdot1.5\text{CH}_2\text{Cl}_2$ (**1**·$1.5\text{CH}_2\text{Cl}_2$) was isolated from previously reported $\{[\text{Dy}(\text{L}^{\text{N6en}})(\text{CH}_3\text{COO})_2](\text{NO}_3)\}\cdot2\text{H}_2\text{O}$,[25] through a modified version of a published method,[37,38] as illustrated in Fig. 1.

Recrystallisation of the isolated solid by diffusion of diethyl ether into a dichloromethane solution of the complex at *ca.* 5 °C allowed to collection of colourless single crystals of $\{[\text{Dy}(\text{L}^{\text{N6en}})(\text{OSiPh}_3)_2](\text{BPh}_4)\}\cdot1.5\text{CH}_2\text{Cl}_2$ (**1**·$1.5\text{CH}_2\text{Cl}_2$). This compound is stable in air, as no significant changes were observed in the experimental powder X-ray diffractogram (Fig. S1†) or in its elemental analyses after one year. Moreover, no noticeable changes in colour or appearance were observed upon exposure to air over the same period.

The diluted $\{[\text{Dy}_{0.1}\text{Y}_{0.9}(\text{L}^{\text{N6en}})(\text{OSiPh}_3)_2](\text{BPh}_4)\}\cdot1.5\text{CH}_2\text{Cl}_2$ (**1@Y**·$1.5\text{CH}_2\text{Cl}_2$) complex was similarly obtained, by mixing

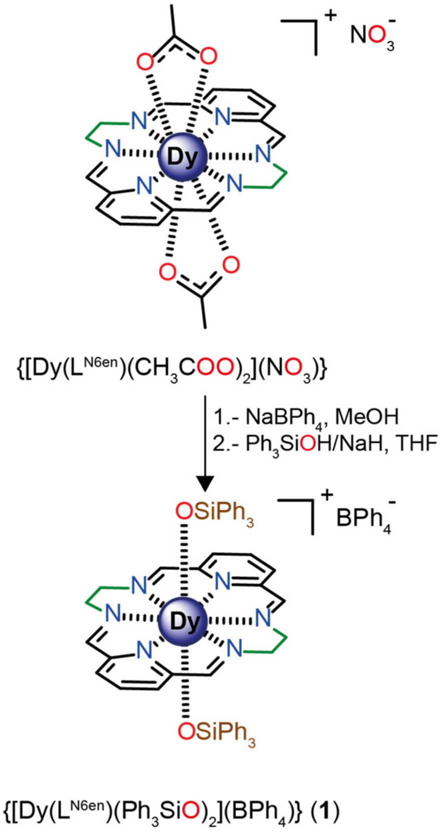

Fig. 1 Reaction scheme for the isolation of **1** from related $\{[\text{Dy}(\text{L}^{\text{N6en}})(\text{CH}_3\text{COO})_2](\text{NO}_3)\}$. Solvate molecules are omitted for clarity.

dysprosium and yttrium species in the adequate ratios (see ESI†). The composition and purity of the yttrium species was checked by elemental analysis and ^{1}H NMR spectroscopy (ESI†). The Dy : Y proportion for **1@Y**·1.5CH_2Cl_2 was corroborated by micro X-ray fluorescence techniques.

The experimental data for the X-ray diffraction studies of **1**·1.5CH_2Cl_2 are summarised in Table S1.† The asymmetric unit of **1**·1.5CH_2Cl_2 contains two crystallographically different, but chemically equivalent, halves of the cationic complex $[Dy(L^{N6en})(OSiPh_3)_2]^+$, whose metal atoms are sited on inversion centres, and a whole $[BPh_4]^-$ anion. Consequently, the two whole complex molecules, which will be called **1a** and **1b**, are respectively generated by the symmetry operations ($-x + 2$, $-y + 2$, $-z$) and ($-x + 1$, $-y + 1$, $-z + 1$). Ellipsoid diagrams of the cations of these two molecules are shown in Fig. 2 and S2,† respectively. Moreover, the asymmetric unit includes disordered molecules of dichloromethane as solvate, summing up to 1.5 molecules per complex unit. In addition to the disorder shown by the solvates, for cation **1b** (which contains Dy2), some atoms (N21, N23 and the contiguous ethylene chains) are also disordered on two sites (occupation sites 0.51 : 0.49).

The cationic complex $[Dy(L^{N6en})(OSiPh_3)_2]^+$ displays an N_6O_2 coordination environment, similar to those observed for other octacoordinated dysprosium complexes derived from N_6 macrocycles (Table S2†),[39] with $\{[Dy(L^8)(Ph_3SiO)_2](BPh_4)\}$[38] ($L^8$ = (2*E*,6*E*,9*E*,13*E*)-2,7,9,14-tetramethyl-3,6,10,13-tetraaza-1,8 (2,6)-dipyridinacyclotetradecaphane-2,6,9,13-tetraene) being particularly alike, since the main difference with **1** is the presence of methyl groups on the imine carbon atoms of L^8. Calculations of the degree of distortion of the DyN_6O_2 core relative to an ideal polyhedron of eight vertexes made for **1** with the SHAPE program[40,41] (Table S3†), reveal a hexagonal bipyramid (hbp) geometry. The neutral N_6 donor macrocycle lies in the equatorial plane, with both triphenylsilanolate anions occupying opposite apical positions with a perfect O-Dy-O angle of 180°. With such low distortion of the polyhedron, Dy1 is contained in the calculated plane formed by the six N-donor atoms, while these latter ones only protrude *ca.* 0.15 Å from the calculated plane. It is remarkable that the deviation from an ideal hbp is also notably smaller for **1** (Table S2†) than for the mentioned $\{[Dy(L^8)(Ph_3SiO)_2](BPh_4)\}$,[38] since its ChSM value is 2.163, while this value is between 1.12 and 1.44 for **1**. The main geometric parameters of this compound are listed in Table S4,† with typical values, including both coordination Dy–O and Dy–N distances, which are within the usual ranges found for other related compounds.[39]

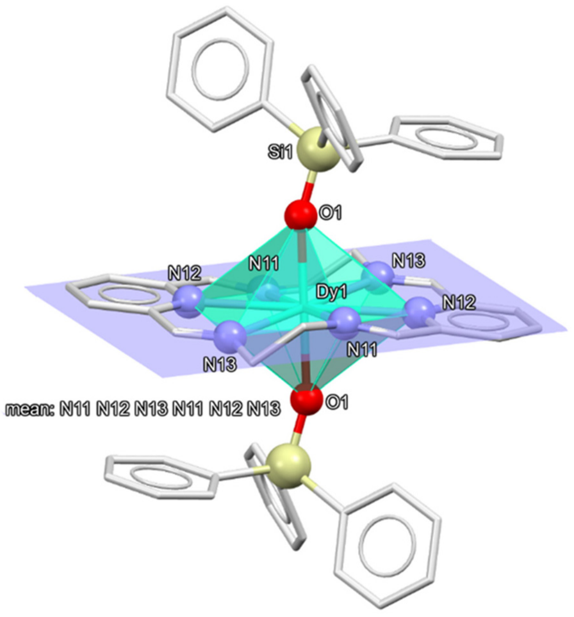

Fig. 2 Balls and sticks diagram for the cation $[Dy(L^{N6en})(OSiPh_3)_2]^+$ in the $\{[Dy(L^{N6en})(OSiPh_3)_2](BPh_4)\}$ complex **1a**, showing Dy1 as a polyhedron. Only heteroatoms of the asymmetric unit and those corresponding to the coordination sphere are labelled.

Powder X-ray diffraction measurements for **1**·1.5CH_2Cl_2 (Fig. S1†) reveal that the isolated product was obtained with high purity, as no additional peaks were observed in the experimental diffractogram. Furthermore, the diffractogram of the complex was remeasured after one year, demonstrating that both patterns are equal. These results confirm the air stability of the compound, without detecting any sign of decomposition.

In addition, the powder X-ray diffractogram for the diluted analogue **1@Y**·1.5CH_2Cl_2 (Fig. S3†) agrees with a very similar structure to that of **1**·1.5CH_2Cl_2.

Magnetic studies

Direct-current (dc) magnetic susceptibility measurements for **1**·1.5CH_2Cl_2 were recorded in the 2–300 K temperature range. The $\chi_M T$ *vs.* T graph is shown in Fig. S4.† The $\chi_M T$ value at 300 K is 14.4 cm^3 K mol^{-1}, which is close to the expected one for an uncoupled Dy^{3+} ion at room temperature (14.17 cm^3 K mol^{-1}). The experimental curve remains basically constant up to 15 K, and then it drops sharply, to reach a value of 4.8 cm^3 K mol^{-1} at 2 K. This great drop seems to indicate magnetic blocking more than the presence of large crystal field splitting.[35] In fact, *ab initio* calculations (*vide infra*), which take into account the large crystal field, do not show such sharp drop at low T (Fig. S4†). The field dependence of the reduced magnetisation at 2 K at the maximum applied field of 5 T tends to 5.5 $N\mu_\beta$, suggesting a highly anisotropic Dy^{3+} ion with an Ising-like ground doublet.[42] Moreover, the magnetisation graph shows a sigmoidal shape at low field, which is often found for high-performance SMMs.[35,43]

The dynamic magnetic properties of **1**·1.5CH_2Cl_2 were also studied, and they show out-of-phase frequency dependence of the susceptibility (χ''_M) as a function of the temperature up to 100 K (Fig. 3).

In addition, the Cole–Cole plots (Fig. S5†) display curves with α parameters in the range 0.3–0.1 (Table S5†), indicative of various relaxation processes.[37,44] The presence of multiple relaxation mechanisms is also supported by the dependence

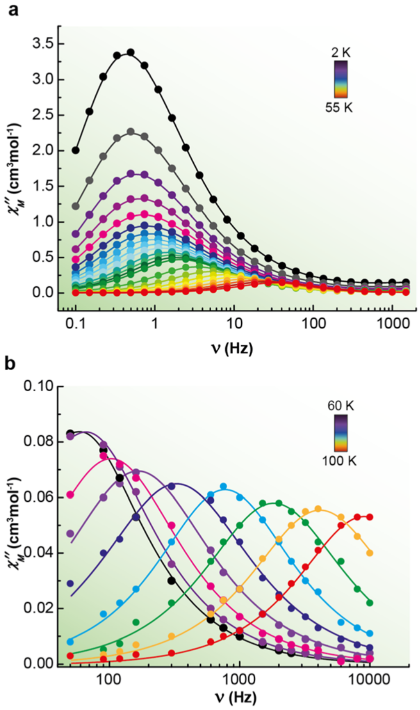

Fig. 3 Frequency dependence of χ''_M for $\mathbf{1}\cdot1.5CH_2Cl_2$ at H_{dc} = 0 at frequencies ranging from: (a) 0.1 to 1500 Hz; (b) 50 to 10 000 Hz. Solid lines are fits to the data.

of the relaxation time τ with temperature in the 2–100 K range (Fig. 4), which shows varying behaviour across different temperature ranges. Thus, below 10 K, the relaxation is almost independent of temperature and this behaviour points out to a quantum tunnelling of magnetisation (QTM) mechanism. Above this temperature, the shape of the curve is in agreement with the presence of thermally activated processes.[32]

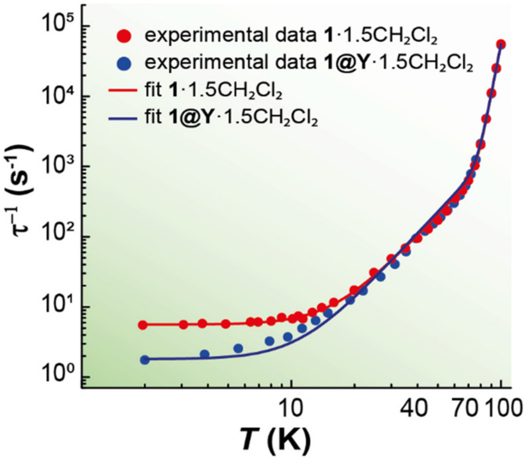

Fig. 4 Dependence of the relaxation rate with temperature for $\mathbf{1}\cdot1.5CH_2Cl_2$ (red solid circles) and $\mathbf{1@Y}\cdot1.5CH_2Cl_2$ (blue solid circles). The red and blue solid lines account for the best fits considering Orbach, Raman and QTM relaxation processes.

Hence, attempts were made to fit this plot considering all the possible relaxation mechanisms except the Direct one (Orbach, Raman, and QTM), according to eqn (1), individually or grouped.

$$\frac{1}{\tau}=\frac{1}{\tau_0}e^{\left(\frac{-U_{\mathrm{eff}}}{k_B T}\right)}+CT^n+\frac{1}{\tau_{\mathrm{QTM}}} \qquad (1)$$

The best fit of the data (Fig. 4) is obtained considering the three relaxation processes, and this renders the parameters $U_{\mathrm{eff}} = (1528 \pm 6)$ K [(1062 ± 4) cm^{-1}], $\tau_0 = (6.9 \pm 0.3) \times 10^{-11}$ s, $C = (8.5 \pm 0.1) \times 10^{-4}$ s^{-1} K^{-n}, $n = (3.2 \pm 0.2)$ and $\tau_{\mathrm{QTM}} = (0.2 \pm 0.1)$ s. The n value can seem quite low, but considerations of both the acoustic and optical phonons in magnetic dynamics can explain the deviation from the predicted value for the Kramers ion (n = 9).[45,46]

The comparison of these data with those obtained for some magneto-structurally characterised mononuclear dysprosium SMMs with N_6 macrocycles and triphenylsilanolate as ligands (Table S2†)[35,38,43,47] allows to draw some conclusions. Thus, comparison between $\mathbf{1}\cdot1.5CH_2Cl_2$ and $\{[Dy(L^8)(Ph_3SiO)_2](BPh_4)\}$[38] clearly shows that removing an electron-donating group from the N_6 macrocyclic ligand, such as the methyl one, significantly improves the energy barrier for the spin reversal. From this, $\mathbf{1}\cdot1.5CH_2Cl_2$ has a barrier of *ca.* 1500 K, while for $\{[Dy(L^8)(Ph_3SiO)_2](BPh_4)\}$ U_{eff} is *ca.* 1100 K.[38] The absence of the methyl groups in $\mathbf{1}\cdot1.5CH_2Cl_2$ results in a more perfect hbp polyhedron. However, this less deviated geometry does not explain by itself the improved results, as Table S2† evidences. Accordingly, this work deepens in the fact that the elimination of electron-donating substituents in the equatorial plane is a key factor in enhancing the behaviour of SMMs, as previously inferred.[39]

Variable-field magnetisation measurements revealed the trends in magnetic relaxation behaviour. The data were recorded by scanning the field between −3 and 3 T, employing an average sweep rate of 10 mT s^{-1}. At low temperatures, the magnetisation value experiences a steep decline close to H = 0 (Fig. 5a) but with open curves, which also suggests the existence of fast QTM relaxation. This relaxation mechanism is common among dysprosium hexagonal bipyramidal SMMs (Table S2†). In spite of this, the complex shows open thin hysteresis till 12 K (Fig. 5a and b). The blocking temperature T_B^H was established by observing the last temperature at which the remanent magnetisation decreases, a criterion commonly used[32,48] to establish the T_B^H values in different SMMs. The low values of magnetisation and coercive field cannot be attributed to artefacts due to errors in measures, given that the field was corrected using a palladium standard measured under the same conditions.

In addition, zero-field-cooled (ZFC) and field-cooled (FC) magnetic susceptibility curves show divergence up to 10 K (Fig. S6†), supporting the hysteresis results.

An yttrium magnetically diluted mixed compound $\{[Dy_{0.1}Y_{0.9}(L^{N6en})(OSiPh_3)_2](BPh_4)\}\cdot1.5CH_2Cl_2$ ($\mathbf{1@Y}\cdot1.5CH_2Cl_2$) was also synthesized in order to improve the magnetic block-

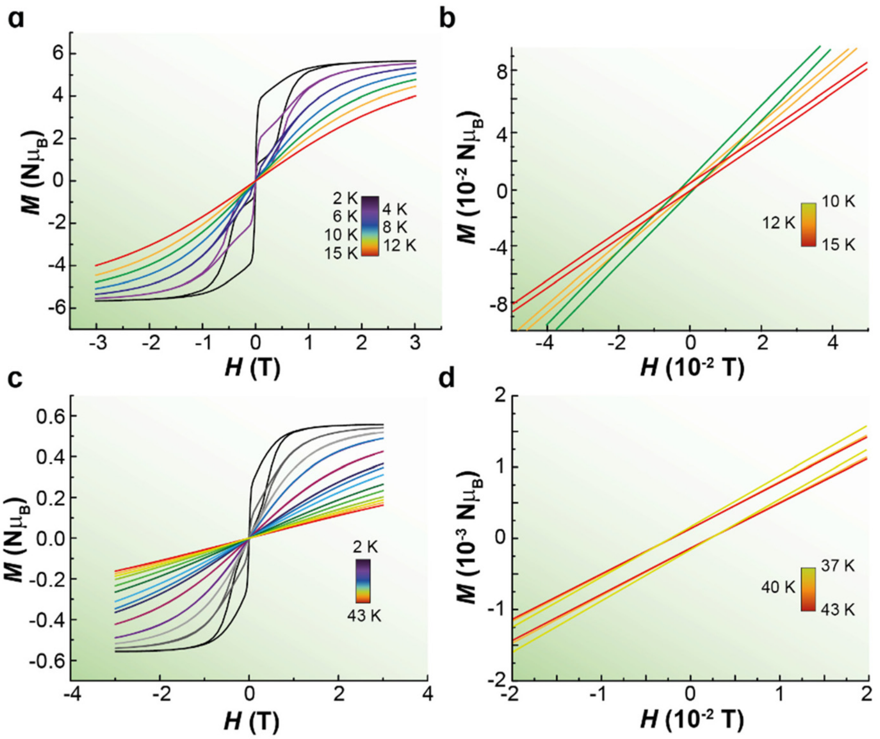

Fig. 5 (a) Magnetic hysteresis measurements for **1**·1.5CH$_2$Cl$_2$ collected at 2–15 K with an average sweep rate of 10 mT s^{-1}. (b) Expansion of the region near zero field at 10–15 K. (c) Magnetic hysteresis measurements for **1@Y**·1.5CH$_2$Cl$_2$ collected at 2–43 K with an average sweep rate of 10 mT s^{-1}. (d) Expansion of the region near zero field at 37–43 K.

ing. The relaxation times (Fig. 4) extracted from the χ''_M *vs.* ν graph (Fig. S7†) for **1@Y**·1.5CH$_2$Cl$_2$ closely overlap with those of **1**·1.5CH$_2$Cl$_2$ above 20 K (Fig. 4). However, below 20 K, both curves differ significatively and the one for **1@Y**·1.5CH$_2$Cl$_2$ shows a gradual but more pronunced drop of the τ^{-1} values with temperature compared to **1**·1.5CH$_2$Cl$_2$. This could suggets a reduction of the QTM. Nevertheless, the Cole–Cole plots (Fig. S8†) and the dependence of τ with temperature still agree with various relaxations mechanism. Thus, the best fitting of the relaxation times for the diluted complex renders the parameters $U_{\text{eff}} = (1531 \pm 5)$ K [(1064 ± 2) cm^{-1}], $\tau_0 = (4.3 \pm 0.1) \times 10^{-12}$ s, $C = (5.7 \pm 0.5) \times 10^{-5}$ s^{-1} K^{-n}, $n = (3.8 \pm 0.2)$ and $\tau_{\text{QTM}} = (0.6 \pm 0.2)$ s. Accordingly, it seems that the dilution partially suppresses the QTM.[49]

The hysteresis cycles recorded for **1@Y**·1.5CH$_2$Cl$_2$ also show thin hysteresis, with open loops up to 40 K (Fig. 5c and d). Consequently, the diminishment of the QTM in the diluted sample seems to result in a significant improvement in the blocking temperature. However, the observed enhancement might also be partly driven by changes in the Raman relaxation mechanism, the mitigation of which generally leads to an improvement in the magnetic properties.[50]

FC/ZFC measurements for **1@Y**·1.5CH$_2$Cl$_2$ also reveal divergences in the curves up to 40 K (Fig. S9†), though no clear peaks are present. A similar absence of peaks was noted by Coronado in the encapsulated stable molecule magnet with T_B^H of 39 K, which also exhibits thin magnetic hysteresis.[32]

Therefore, the FC/ZFC measurements also support the hysteresis results. Consequently, to the best of our knowledge, the blocking temperature for **1@Y**·1.5CH$_2$Cl$_2$ exceeds the reported highest T_B^H of 36 K (sweep rate 20 mT s^{-1}) for uncapsulated, air-stable SMMs, establishing a new record.

Ab initio calculations

Multiconfigurational SA-CASSCF calculations[51] with the SINGLE_ANISO code,[52] as implemented in Orca 5.0.3,[53–55] have been performed to gain more insight into the magnetic properties of **1**. The atom coordinates of both complex units present in the crystal structure have been employed. In the case of **1b**, due to the disorder of the experimental geometry, two models have been created (**1b_1** and **1b_2**, see computational details in ESI and Fig. S10†). The results obtained for the three independent calculated molecules are similar, so we have included here only the results for **1a**. Meanwhile, **1b** results are collected in the ESI.† For the Dy^{3+} ion, the ground state $^6H_{15/2}$ is formed by eight Kramers Doublets (KDs). For **1a** the KDs span in an energy range of about 1450 cm^{-1} (Table 1). Analysis of the KDs and their *g*-factors reveals a very large easy-axis anisotropy in the complex (Tables 1, S6 and S7†).

The ground state KD is $m_J = |\pm 15/2\rangle$, which is highly anisotropic, and it is characterised by a large axial *g* component and a small transverse one. The anisotropy g_{zz} axis for **1a** lies mostly along the O–Dy–O direction, as shown in Fig. 6a.

Table 1 Information of the eight low-lying KDs calculated at CASSCF level. Relative energies (in cm^{-1}), components of the g-tensor, and tilting angle (θ) of the g_{zz} component of the corresponding excited state KD with respect to the ground state KD for **1a**

Energy (cm^{-1})	g_{xx}	g_{yy}	g_{zz}	θ (°)
0	0.00025	0.00027	19.883	
519.9	0.066	0.068	16.973	4.712
941.6	0.007	0.081	14.004	7.198
1206.6	1.343	1.532	9.238	12.346
1296.3	1.597	8.440	10.993	85.867
1323.6	1.148	6.988	11.265	86.580
1375.9	1.315	2.223	7.640	88.050
1443.1	0.563	7.319	12.239	80.777

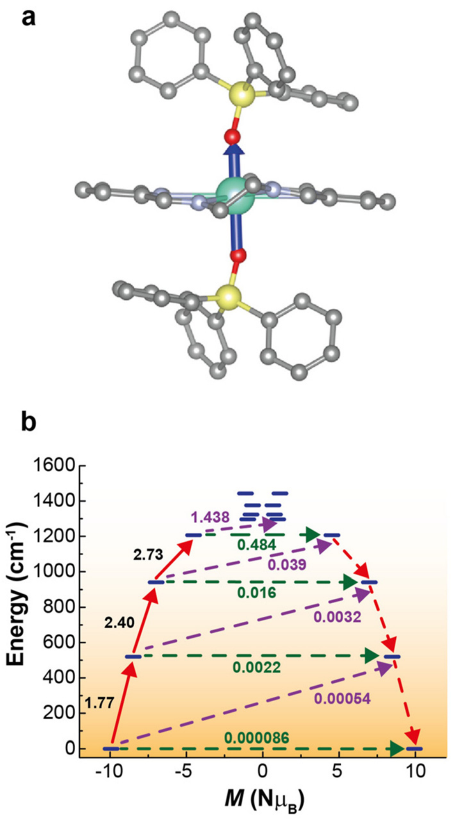

Fig. 6 (a) Ball and stick representation of the molecular structure for **1a** with the calculated orientation of the main magnetic axis of the ground Kramers doublet. Dysprosium, silicon, oxygen, nitrogen and carbon are represented in cyan, yellow, red, light blue and grey, respectively. Hydrogen atoms are omitted for clarity. (b) State energies as a function of their average magnetic moment, M, along the main anisotropy axis for **1a** obtained with SINGLE-ANISO. The dashed green arrows correspond to the quantum tunnelling mechanism of ground or excited states, dashed purple arrow shows the hypothetical Orbach relaxation process. The solid red arrow indicates the transition between the ground and excited Kramers doublets, and the dashed red arrow the excitation pathway to the ground state with the reversed spin. The values close to the arrows indicate the matrix elements of the transition magnetic moments (above 0.1 an efficient spin relaxation mechanism is expected).

The first and second excited KDs are also highly anisotropic with large axial g components. Additionally, for the first and second excited KDs, the g_{zz} axis are aligned close (tilting angles smaller than 8°) to the ground state one, decreasing the probability of relaxation through those states. Moreover, the *ab initio* blocking barrier has been computed (Fig. 6b), suggesting that relaxation occurs through the third excited state, located around 1200 cm^{-1}, close to the experimental value of 1062 cm^{-1}.

Quite similar results were observed for **1b** (see Tables S6, S7, Fig. S11 and S12†), demonstrating that *ab initio* calculations support the experimentally found energy barrier.

Photoluminescence and luminescence thermometry

To assess the potential of the prepared SMMs as thermographic materials, the temperature-dependent solid-state emission spectra of **1**·1.5CH$_2$Cl$_2$ and **1@Y**·1.5CH$_2$Cl$_2$ were acquired upon excitation at 364 and 461 nm, respectively (corresponding to the maxima observed in their excitation spectra, Fig. S13†). A significant influence of dilution on the luminescence was observed, as discussed below.

For **1**·1.5CH$_2$Cl$_2$, the emission spectrum (Fig. S14a†) exhibits characteristic Dy^{3+} intra-4f transitions (^{4}F$_{9/2}$ → ^{6}H$_{11/2}$, ^{4}F$_{9/2}$ → ^{6}H$_{13/2}$, and ^{4}F$_{9/2}$ → ^{6}H$_{15/2}$) at approximately 659, 590, and 488 nm, respectively. These transitions, however, display low relative intensity and are only observed up to 145 K. Additionally, a broad band in the UV-visible spectral range (380–550 nm) attributed to ligand-based emission[25] dominates the spectra across the entire temperature range. At low temperatures, this band is significantly intense and quenches as the temperature rises (Fig. S14a†).

To explore this temperature-dependent behaviour for luminescence thermometry, the ratio of the integrated areas I_1 (ligand), I_2 (^{4}F$_{9/2}$ → ^{6}H$_{15/2}$), and I_3 (^{4}F$_{9/2}$ → ^{6}H$_{13/2}$), $\Delta_1 = (I_2 + I_3)/I_1$, was employed as the thermometric parameter (Fig. S14b and c†). As temperature increases, Δ_1 decreases, indicating the potential of **1**·1.5CH$_2$Cl$_2$ as a luminescent thermometer in the 13–120 K range. A phenomenological linear calibration curve was fitted to the data (Fig. S14c†), with the corresponding parameters summarized in Table S8.† The thermometric performance was further evaluated using the relative thermal sensitivity (S_r) and temperature uncertainty (δT), the standard figures of merit for luminescent thermometers (see ESI for details†).[56] A maximum S_r of 3.5% K^{-1} and a minimum δT of 3.0 K at 120 K were obtained (Fig. S14d, e and Table S8†). These results show a modest thermometric performance. However, they also validate the viability of **1**·1.5CH$_2$Cl$_2$ as a functional luminescent thermometer, capable of providing approximate temperature monitoring within the studied range, despite this range being above the magnetic blocking temperature of **1**·1.5CH$_2$Cl$_2$, 12 K (as it occurs for all reported SMMs). Even so, this is the SMM with the highest effective energy barrier and blocking temperature for which luminescent thermometry has been observed, the previous records being at 994 K and 8 K, respectively.[23]

Since **1@Y**·1.5CH$_2$Cl$_2$ exhibits a blocking temperature of 40 K, its temperature-dependent luminescence was also evaluated and, as discussed below, the results demonstrate that it is the first SMM operating as a luminescent thermometer below its blocking temperature.

The emission spectra of **1@Y**·$1.5CH_2Cl_2$ show a broad emission band centred at 575 nm (Fig. 7a), indicative of ligand-based luminescence. Although this band may appear red-shifted compared to that of the undiluted complex **1**·$1.5CH_2Cl_2$, the shift arises from the use of a different excitation wavelength (461 nm) to maximize emission. When both spectra are recorded under identical excitation conditions (364 nm), the broad emission bands are centred at the same wavelength (Fig. S15†), confirming that no actual red shift occurs upon dilution.

In the diluted sample, with only 10% of the metal ion being Dy^{3+}, the signal from Dy^{3+} completely vanishes, thus leaving only the ligand emission observable.[13] Therefore, as the spectra are dominated by a ligand-band emission, the signal is not expected to be influenced by the coercive magnetic field retained in the sample once it is magnetized. Furthermore, excitation at 461 nm prevents efficient energy transfer from the ligand to the Dy^{3+} ion. As a result, the electronic energy levels of the Dy^{3+} centre should remain unaffected by the irradiation, preserving the single-molecule magnet behaviour. Consequently, this selective excitation is particularly advantageous, as it allows for luminescence thermometry to be performed without disturbing the magnetic relaxation dynamics. In contrast to systems where excitation can lead to changes in the population of the 4f electronic states of the lanthanoid ion -thus potentially altering its magnetic anisotropy or inducing changes in the relaxation processes-, this approach minimizes such risks by avoiding direct excitation of Dy^{3+}. Hence, the separation of optical and magnetic pathways in **1@Y**·$1.5CH_2Cl_2$ supports the potential for simultaneous operation of both functionalities.

In an effort to elucidate the underlying mechanism of the emission spectra, time-dependent density functional theory (TDDFT) calculations were performed on the X-ray structure of **1**·$1.5CH_2Cl_2$ using hybrid correlation and exchange functionals like B3LYP[57] or PBE0.[58] However, these functionals, commonly used for such studies, yielded unrealistic results, indicating degeneracy of the excited singlet and triplet states.[59] This well-documented issue is often encountered in systems exhibiting long-range charge transfer excitations.[59,60] To better describe long-range interactions, long-range corrected functionals (*e.g.* CAM-B3LYP[61]) or double-hybrid functionals (*e.g.* SCS/SOS-wB2PLYP[62]) are often employed. While these functionals partially alleviate the degeneracy issue for some optimised geometries of the first and fundamental excited states, they still yield unreasonable excitation energies significantly higher than experimental values.

To overcome these limitations, coupled-cluster calculations were performed using the STEOM-DLPNO-CCSD (similarity transformed equation of motion approach combined with the domain-based local pair orbital implementation of coupled-cluster singles and doubles) method[54,63–68] implemented in Orca 5.0.3.[53–55] This methodology does not present the problems of the TDDFT with the charge transfer excitations but is

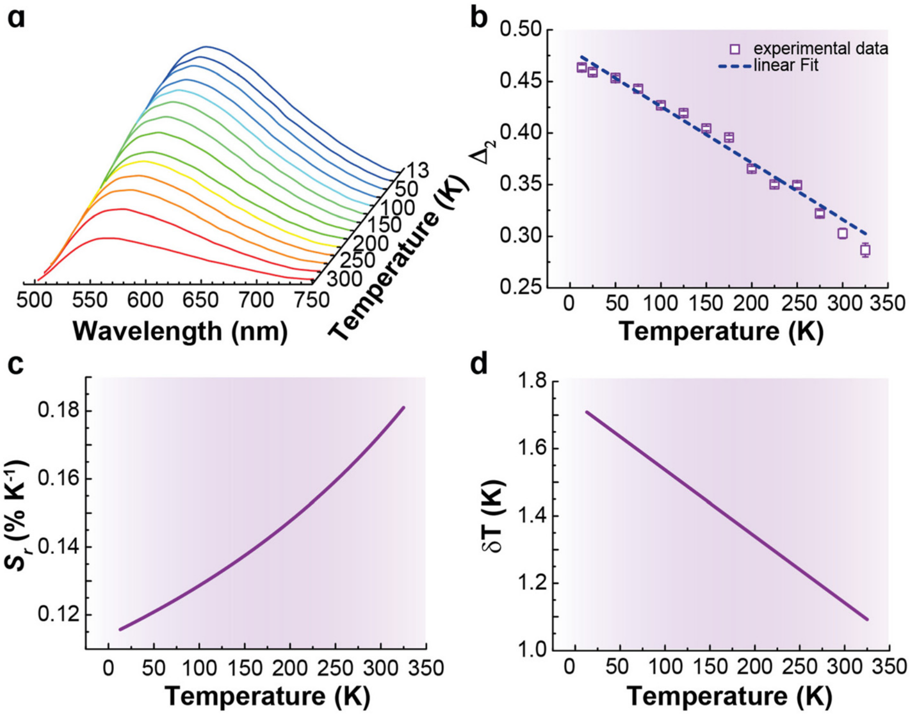

Fig. 7 (a) Temperature-dependent emission spectra of **1@Y**·$1.5CH_2Cl_2$ excited at 461 nm. (b) Temperature dependence of the thermometric parameter (Δ_2) for **1@Y**·$1.5CH_2Cl_2$. The line represents the best linear fit ($r^2 > 0.98$) to the experimental data (fit details provided in Table S8†). (c) Temperature dependence of S_r for **1@Y**·$1.5CH_2Cl_2$. (d) Temperature dependence of δT for **1@Y**·$1.5CH_2Cl_2$.

computationally demanding, limiting its applicability to smaller systems, preventing the calculation of the complete lanthanoid complex. Thus, the ligands L^{N6en}, Ph_3SiO^- and the counterion BPh_4^- were analysed separately. The STEOM-DLPNO-CCSD results (Table S9†) show that the lowest singlet excitation originates from the axial Ph_3SiO^- ligand (309 nm), while the lowest-energy triplet emission arises from the equatorial ligand (423 nm). These results qualitatively agree with experimental observations, suggesting a possible charge transfer between the two ligands, consistent with the difficulties encountered in TDDFT calculations. They also suggest that BPh_4^- is unlikely to participate directly in a charge transfer process with the ligands, given that its first singlet excited state appears at significantly higher energy (261 nm). While the STEOM-DLPNO-CCSD calculations provide a reasonable description, considering the limitations of calculating the complete system, a quantitative reproduction of experimental data remains challenging. Accordingly, the temperature dependence of the emission spectra of **1@Y**·1.5CH_2Cl_2 can be explained by two distinct ligand-based components. To quantify these contributions, we employed a deconvolution technique with two Gaussian components (Fig. S16a†). The resulting fitting parameters (peak energy, width, and integrated area) are summarized in Table S10 in ESI.† Notably, while peak energy and width remain constant, the integrated area of each component (A_1 and A_2) decreases with increasing temperature (Fig. S16b†). This suggests a temperature-dependent variation in the relative intensities of these ligand-based emissions. Therefore, to demonstrate the applicability of **1@Y**·1.5CH_2Cl_2 as a ratiometric luminescent thermometer, we employed the ratio of the integrated areas of the two Gaussian components ($\Delta_2 = A_1/A_2$, Fig. 7b). In the absence of a theoretical framework for this ratio, a phenomenological linear calibration curve was established (parameters in Table S8 of the ESI†) and the thermometric performance was evaluated using S_r and δT values. **1@Y**·1.5CH_2Cl_2 operates as a luminescent thermometer in the 13–325 K temperature range. While the maximum S_r (0.2% K^{-1}) and minimum δT (1.0 K), both at 325 K, are not exceptional (Fig. 7c and d), they are comparable to other broadband emission materials.[56]

Despite this, the relatively low uncertainty (below 1.7 K across the entire temperature range) allows for temperature monitoring of cryogenic magnets, indicating that **1@Y**·1.5CH_2Cl_2 is a luminescent thermometer below its T_B^H (40 K). Thus, **1@Y**·1.5CH_2Cl_2 represents a dual magneto-optical molecule, capable of self-monitoring its temperature, and this advancement helps address the challenge of temperature monitoring in molecular magnetic nanomaterials where conventional thermometers are impractical, in order to avoid their loss of magnetization.

Conclusions

This work, which reports a high-performance mononuclear SMM (**1**·1.5CH_2Cl_2) and its yttrium diluted analogue (**1@Y**·1.5CH_2Cl_2), unveils the first SMM capable of self-monitoring temperature within the range where it acts as a magnet. Significantly, **1@Y**·1.5CH_2Cl_2 is an air-stable SMM that exhibits a blocking temperature of 40 K, the highest T_B^H among uncapsulated air-stable molecule magnets reported to date. The integration of luminescence thermometry and magnet performance in this diluted material, with a high energy barrier (>1000 cm^{-1}), is achieved through a meticulous design that separates the origin of the magnetic properties, which relies on Dy^{3+} ions, from the luminescence, that is based on the emitting ligands. This approach diverges from conventional SMMs, where the lanthanoid ion contributes to both functions, often limiting the potential for high-performance luminescent magnets. Our strategy, exemplified by **1@Y**·1.5CH_2Cl_2, overcomes this limitation, and provides a route for non-invasive optical interrogation of the material, enabling temperature readout without compromising the magnetic state. This separation of optical and magnetic pathways supports the simultaneous operation of both functionalities. Besides, **1@Y**·1.5CH_2Cl_2 holds the distinction of being the SMM with the highest energy barrier and blocking temperature reported to date while simultaneously enabling self-temperature monitoring through luminescence thermometry.

Rigorous theoretical calculations, including innovative coupled cluster methods for luminescence analysis (instead of the more commonly used time-dependent DFT ones), provide robust support for the experimental magnetic and luminescent data.

As a result, this work sets a new standard for designing SMMs with enhanced integrated luminescence thermometry. Future research will focus on refining this strategy through ligand optimization to achieve even higher operational temperatures. Subtle modifications to the ligand can influence the coordination environment of the lanthanoid ions, resulting in increased magnetic anisotropy, and the material's luminescent properties, enhancing overall performance and functionality.

Author contributions

Conceptualization: M. F., J. C.-V., E. R., L. D. C.; methodology: J. C.-V., C. G.-B., J. S.-M., S. G.-C.; validation: M. F., E. R., L. D. C.; formal analysis: J. C.-V., M. F., A. M. G.-D., S. G.-C., E. R., C. D. S. B.; investigation: J. C.-V., C. G.-B.; resources: M. F., E. R., L. D. C.; visualization: J. C.-V., C. G.-B., S. G.-C., C. D. S. B.; data curation and supervision: M. F., E. R., L. D. C.; writing – original draft preparation: M. F., J. C.-V., E. R., S. G.-C., L. D. C.; project administration: M. F., L. D. C.; funding acquisition: M. F., E. R., L. D. C.

Data availability

The data supporting this article have been included as part of the ESI.†

Crystallographic data for **1**·1.5CH$_2$Cl$_2$ have been deposited with The Cambridge Crystallographic Data Centre (CCDC 2262113†).

Conflicts of interest

There are no conflicts to declare.

Acknowledgements

This work was supported by Universidade de Santiago de Compostela (2024-PU027-1), Consellería de Cultura, Educación, Formación Profesional e Universidades, Xunta de Galicia (convenio 2023-1298), by Portuguese funds through the FCT/MCTES (PIDDAC) (UIDB/50011/2020, **https://doi.org/10.54499/UIDB/50011/2020**; UIDP/50011/2020, **https://doi.org/10.54499/UIDP/50011/2020**; and LA/P/0006/2020, **https://doi.org/10.54499/LA/P/0006/2020** projects of the CICECO-Aveiro Institute of Materials), and by Ministerio de Ciencia, Innovación y Universidades (PID2021-122464NB-I00 and Maria de Maeztu CEX2021-001202-M). This article is based upon work from COST Action CA22131, supported by COST (European Cooperation in Science and Technology). J. C. V. also thanks Xunta de Galicia for his postdoctoral fellowship (ED481B-2022-068). We also acknowledge the Generalitat de Catalunya for the 2021-SGR-00286 grant and E. R. for an ICREA Academia grant. We thank CSUC and BSC supercomputer centres for the computational resources.

References

1 R. Sessoli, Single-atom data storage, *Nature*, 2017, **543**, 189–190.
2 A. Gaita-Ariño, F. Luis, S. Hill and E. Coronado, Molecular spins for quantum computation, *Nat. Chem.*, 2019, **11**, 301–309.
3 M. Atzori and R. Sessoli, The Second Quantum Revolution: Role and Challenges of Molecular Chemistry, *J. Am. Chem. Soc.*, 2019, **141**, 11339–11352.
4 R. Marin, G. Brunet and M. Murugesu, Shining New Light on Multifunctional Lanthanide Single-Molecule Magnets, *Angew. Chem., Int. Ed.*, 2021, **60**, 1728–1746.
5 A. G. Bispo-Jr, Multifunctional lanthanide(III) single-molecule magnets displaying luminescence thermometry: Progress, challenges, and future directions, *Coord. Chem. Rev.*, 2025, **537**, 216685.
6 G. Brunet, R. Marin, M.-J. Monk, U. Resch-Genger, D. A. Gálico, F. A. Sigoli, E. A. Suturina, E. Hemmer and M. Murugesu, Exploring the dual functionality of an ytterbium complex for luminescence thermometry and slow magnetic relaxation, *Chem. Sci.*, 2019, **10**, 6799–6808.
7 D. Errulat, R. Marin, D. A. Gálico, K. L. M. Harriman, A. Pialat, B. Gabidullin, F. Iikawa, O. D. D. Couto Jr., J. O. Moilanen, E. Hemmer, F. A. Sigoli and M. Murugesu, A luminescent thermometer exhibiting slow relaxation of the magnetization: toward self-monitored building blocks for next-generation optomagnetic devices, *ACS Cent. Sci.*, 2019, **5**, 1187–1198.
8 D. A. Gálico, R. Marin, G. Brunet, D. Errulat, E. Hemmer, F. A. Sigoli, J. O. Moilanen and M. Murugesu, Triplet-State Position and Crystal-Field Tuning in Opto-Magnetic Lanthanide Complexes: Two Sides of the Same Coin, *Chem. – Eur. J.*, 2019, **25**, 14625–14637.
9 K. Kumar, D. Abe, K. Komori-Orisaku, O. Stefańczyk, K. Nakabayashi, J. R. Shakirova, S. P. Tunik and S.-I. Ohkoshi, Neodymium β-diketonate showing slow magnetic relaxation and acting as a ratiometric thermometer based on near-infrared emission, *RSC Adv.*, 2019, **9**, 23444–23449.
10 J. Wang, J. J. Zakrzewski, M. Heczko, M. Zychowicz, K. Nakagawa, K. Nakabayashi, B. Sieklucka, S. Chorazy and S.-I. Ohkoshi, Proton conductive luminescent thermometer based on near-infrared emissive {YbCo$_2$} molecular nanomagnets, *J. Am. Chem. Soc.*, 2020, **142**, 3970–3979.
11 M. Fondo, J. Corredoira-Vázquez, A. M. García-Deibe, J. Sanmartín-Matalobos, M. Amoza, A. M. P. Botas, R. A. S. Ferreira, L. D. Carlos and E. Colacio, Field-induced slow magnetic relaxation and luminescence thermometry in a mononuclear ytterbium complex, *Inorg. Chem. Front.*, 2020, **7**, 3019–3029.
12 J. Wang, J. J. Zakrzewski, M. Zychowicz, V. Vieru, L. F. Chibotaru, K. Nakabayashi, S. Chorazy and S.-I. Ohkoshi, Holmium(III) molecular nanomagnets for optical thermometry exploring the luminescence re-absorption effect, *Chem. Sci.*, 2021, **12**, 730–741.
13 S. Ma, T. Zhang, J.-P. Zhao, Z.-Y. Liu and F.-C. Liu, A magnetic site dilution approach to achieve bifunctional fluorescent thermometers and single-ion magnets, *Dalton Trans.*, 2021, **50**, 1307–1312.
14 A. A. Kitos, D. A. Gálico, N. Mavragani, R. Castañeda, J. O. Moilanen, J. L. Brusso and M. Murugesu, Probing optical and magnetic properties via subtle stereoelectronic effects in mononuclear DyIII-complexes, *Chem. Commun.*, 2021, **57**, 7818–7821.
15 R. A. S. Ferreira, E. Mamontova, A. M. P. Botas, M. Shestakov, J. Vanacken, V. Moshchalkov, Y. Guari, L. F. Chibotaru, D. Luneau, P. S. André, J. Larionova, J. Long and L. D. Carlos, Synchronous temperature and magnetic field dual-sensing by luminescence in a dysprosium single-molecule magnet, *Adv. Opt. Mater.*, 2021, **9**, 2101495.
16 R. Marin, D. A. Gálico, R. Gayfullina, J. O. Moilanen, L. D. Carlos, D. Jaque and M. Murugesu, A zero-field single-molecule magnet with luminescence thermometry capabilities containing soft donors, *J. Mater. Chem. C*, 2022, **10**, 13946–13953.
17 V. Tangoulis, V. Nastopoulos, N. Panagiotou, A. Tasiopoulos, G. Itskos, M. Athanasiou, E. Moreno-Pineda, W. Wernsdorfer, M. Schulze and O. Malina, High-performance luminescence thermometer with field-

induced slow magnetic relaxation based on a heterometallic cyanido-bridged 3d–4f complex, *Inorg. Chem.*, 2022, **61**, 2546–2557.

18 K. Karachousos-Spiliotakopoulos, V. Tangoulis, N. Panagiotou, A. Tasiopoulos, V. Nastopoulos, E. Moreno-Pineda, W. Wernsdorfer, M. Schulze, A. M. P. Botas and L. D. Carlos, Lanthanide luminescence thermometry and slow magnetic relaxation in 3-D polycyanidometallate-based materials, *Inorg. Chem.*, 2022, **61**, 18629–18639.

19 K. Kumar, O. Stefanczyk, K. Nakabayashi, K. Imoto, Y. Oki and S.-I. Ohkoshi, Detection of sub-terahertz Raman response and nonlinear optical effects for luminescent Yb (III) complexes, *Adv. Opt. Mater.*, 2022, **10**, 2101721.

20 K. Karachousos-Spiliotakopoulos, V. Tangoulis, N. Panagiotou, A. Tasiopoulos, E. Moreno-Pineda, W. Wernsdorfer, M. Schulze, A. M. P. Botas and L. D. Carlos, Luminescence thermometry and field induced slow magnetic relaxation based on a near infrared emissive heterometallic complex, *Dalton Trans.*, 2022, **51**, 8208–8216.

21 J. Corredoira-Vázquez, C. González-Barreira, M. Fondo, A. M. García-Deibe, J. Sanmartín-Matalobos, M. A. Hernández-Rodríguez and L. D. Carlos, Luminescence thermometry in a Dy_4 single molecule magnet, *Dalton Trans.*, 2022, **51**, 15593–15600.

22 J. Wang, J. J. Zakrzewski, M. Zychowicz, Y. Xin, H. Tokoro, S. Chorazy and S.-I. Ohkoshi, Desolvation-induced highly symmetrical terbium(III) single-molecule magnet exhibiting luminescent self-monitoring of temperature, *Angew. Chem., Int. Ed.*, 2023, **62**, e202306372.

23 S. Zanella, M. Aragon-Alberti, C. D. S. Brite, F. Salles, L. D. Carlos and J. Long, Luminescent single-molecule magnets as dual magneto-optical molecular thermometers, *Angew. Chem., Int. Ed.*, 2023, **62**, e202306970.

24 A. G. Bispo-Jr, L. Yeh, D. Errulat, D. A. Gálico, F. A. Sigoli and M. Murugesu, Improving the performance of β-diketonate-based DyIII single-molecule magnets displaying luminescence thermometry, *Chem. Commun.*, 2023, **59**, 8723–8726.

25 J. Corredoira-Vázquez, C. González-Barreira, A. M. García-Deibe, J. Sanmartín-Matalobos, M. A. Hernández-Rodríguez, C. D. S. Brites, L. D. Carlos and M. Fondo, Harnessing ligand design to develop primary and self-calibrated luminescent thermometers with field-induced single ion magnet behaviour in Dy^{3+} complexes, *Inorg. Chem. Front.*, 2024, **11**, 1087–1098.

26 G. Félix, S. Sene, A. Kulakova, A. N. Bilyachenko, V. N. Khrustalev, E. S. Shubina, Y. Guari and J. Larionova, Tetranuclear lanthanide-based silsesquioxanes: towards a combination of a slow relaxation of the magnetization and a luminescent thermometry, *RSC Adv.*, 2023, **13**, 26302–26312.

27 A. G. Bispo-Jr, D. A. Gálico, R. M. Diaz-Rodriguez, J. S. Ovens, F. A. Sigoli and M. Murugesu, The role of terminal ligands in the slow relaxation of magnetisation and luminescence thermometry of dinuclear Nd^{III} complexes, *Inorg. Chem. Front.*, 2023, **10**, 3929–3939.

28 A. G. Bispo-Jr, D. A. Gálico, J. S. Ovens, F. A. Sigoli and M. Murugesu, Impacts of β-diketonate terminal ligands on slow magnetic relaxation and luminescence thermometry in dinuclear Dy^{III} single-molecule magnets, *Dalton Trans.*, 2025, **54**, 4876–4887.

29 S. Shome, N. C. Maurya, M. Mukherjee, K. V. Adarsh and S. Konar, Leveraging ligand conjugation to improve luminescence thermometry in Dy-single-molecule magnets, *Chem. Commun.*, 2025, **61**, 2337–2340.

30 F.-S. Guo, B. M. Day, Y.-C. Chen, M.-L. Tong, A. Mansikkamäki and R. A. Layfield, Magnetic hysteresis up to 80 kelvin in a dysprosium metallocene single-molecule magnet, *Science*, 2018, **362**, 1400–1403.

31 C. A. Gould, K. R. McClain, D. Reta, J. G. C. Kragskow, D. A. Marchiori, E. Lachman, E.-S. Choi, J. G. Analytis, R. D. Britt, N. F. Chilton, B. G. Harvey and J. R. Long, Ultrahard magnetism from mixed-valence dilanthanide complexes with metal-metal bonding, *Science*, 2022, **375**, 198–202.

32 Z. Hu, Y. Wang, A. Ullah, G. M. Gutiérrez-Finol, A. Bedoya-Pinto, P. Gargiani, D. Shi, S. Yang, Z. Shi, A. Gaita-Ariño and E. Coronado, High-temperature magnetic blocking in a monometallic dysprosium azafullerene single-molecule magnet, *Chem*, 2023, **9**, 3613–3622.

33 L. Zhu, Y. Dong, B. Yin, P. Ma and D. Li, Improving the single-molecule magnet properties of two pentagonal bipyramidal Dy^{3+} compounds by the introduction of both electron-withdrawing and -donating groups, *Dalton Trans.*, 2021, **50**, 12607–12618.

34 W.-J. Xu, Q.-C. Luo, Z.-H. Li, Y.-Q. Zhai and Y.-Z. Zheng, Bis-alkoxide dysprosium(III) crown ether complexes exhibit tunable air stability and record energy barrier, *Adv. Sci.*, 2024, **11**, 2308548.

35 Z. Zhu, C. Zhao, T. Feng, X. Liu, X. Ying, X.-L. Li, Y.-Q. Zhang and J. Tang, Air-stable chiral single-molecule magnets with record anisotropy barrier exceeding 1800 K, *J. Am. Chem. Soc.*, 2021, **143**, 10077–10082.

36 M. Suta and A. Meijerink, A Theoretical Framework for Ratiometric Single Ion Luminescent Thermometers—Thermodynamic and Kinetic Guidelines for Optimized Performance, *Adv. Theory Simul.*, 2020, **3**, 2000176.

37 Z.-H. Li, Y.-Q. Zhai, W.-P. Chen, Y.-S. Ding and Y.-Z. Zheng, Air-stable hexagonal bipyramidal dysprosium(III) single-ion magnets with nearly perfect D_{6h} local symmetry, *Chem. – Eur. J.*, 2019, **25**, 16219–16224.

38 A. B. Canaj, S. Dey, E. R. Martí, C. Wilson, G. Rajaraman and M. Murrie, Insight into D_{6h} symmetry: targeting strong axiality in stable dysprosium(III) hexagonal bipyramidal single-ion magnets, *Angew. Chem., Int. Ed.*, 2019, **58**, 14146–14151.

39 J. Corredoira-Vázquez, C. González-Barreira, P. Oreiro-Martínez, A. M. García-Deibe, J. Sanmartín-Matalobos and M. Fondo, Synthesis and applications of lanthanoid complexes of pentadentate and hexadentate N_5 and N_6 macrocycles: A review, *J. Rare Earths*, 2024, **42**, 1–15.

40 M. Llunell, D. Casanova, J. Cirera, P. Alemany and S. Alvarez, *SHAPE, version 2.1*, Universitat de Barcelona, Barcelona, Spain, 2013.

41 A. Ruiz-Martínez, D. Casanova and S. Alvarez, Polyhedral structures with an odd number of vertices: nine-coordinate metal compounds, *Chem. – Eur. J.*, 2008, **14**, 1291–1303.

42 J.-L. Liu, Y.-C. Chen and M.-L. Tong, Symmetry strategies for high performance lanthanide-based single-molecule magnets, *Chem. Soc. Rev.*, 2018, **47**, 2431–2453.

43 S. Liu, Y. Gil, C. Zhao, J. Wu, Z. Zhu, X.-L. Li, D. Aravena and J. Tang, A conjugated Schiff-base macrocycle weakens the transverse crystal field of air-stable dysprosium single-molecule magnets, *Inorg. Chem. Front.*, 2022, **9**, 4982–4989.

44 Y. Guo, K. Liu, Y. Qin, Q. Wu, K. Hu, L. Mei, Z. Chai, X. Liu, J. Yu and W. Shi, Role of molecular symmetry in the magnetic relaxation dynamics of five-coordinate Dy(III) complexes, *Dalton Trans.*, 2023, **52**, 2703–2711.

45 A. Singh and K. N. Shrivastava, Optical-acoustic two-phonon relaxation in spin systems, *Phys. Status Solidi B*, 1979, **95**, 273–277.

46 K. N. Shrivastava, Theory of spin–lattice relaxation, *Phys. Status Solidi B*, 1983, **117**, 437–458.

47 Z. Zhu, C. Zhao, Q. Zhou, S. Liu, X.-L. Li, A. Mansikkamäki and J. Tang, Air-Stable Dy(III)-Macrocycle Enantiomers: From Chiral to Polar Space Group, *CCS Chem.*, 2022, **4**, 3762–3771.

48 S. C. Corner, W. J. A. Blackmore, G. K. Gransbury, A. Mattioni, G. F. S. Whitehead, N. F. Chilton and D. P. Mills, A fluorobenzene-bound dysprosium half-sandwich dication single-molecule magnet, *Chem. Sci.*, 2025, **16**, 610–620.

49 D. S. Krylov, F. Liu, A. Brandenburg, L. Spree, V. Bon, S. Kaskel, A. U. B. Wolter, B. Büchner, S. M. Avdoshenko and A. A. Popov, Magnetization relaxation in the single-ion magnet $DySc_2N@C_{80}$: quantum tunneling, magnetic dilution, and unconventional temperature dependence, *Phys. Chem. Chem. Phys.*, 2018, **20**, 11656–11672.

50 Q.-C. Luo and Y.-Z. Zheng, Mitigating Raman relaxation for high-temperature single-molecule magnets, *Trends Chem.*, 2023, **5**, 869–872.

51 P.-Å. Malmqvist and B. O. Roos, The CASSCF state interaction method, *Chem. Phys. Lett.*, 1989, **155**, 189–194.

52 L. F. Chibotaru and L. Ungur, Ab initio calculation of anisotropic magnetic properties of complexes. I. Unique definition of pseudospin Hamiltonians and their derivation, *J. Chem. Phys.*, 2012, **137**, 064112.

53 F. Neese, Software update: the ORCA program system, version 4.0, *Wiley Interdiscip. Rev.: Comput. Mol. Sci.*, 2018, **8**, e1327.

54 F. Neese, F. Wennmohs, U. Becker and C. Riplinger, The ORCA quantum chemistry program package, *J. Chem. Phys.*, 2020, **152**, 224108.

55 F. Neese, Software update: The ORCA program system—Version 5.0, *Wiley Interdiscip. Rev.: Comput. Mol. Sci.*, 2022, **12**, e1606.

56 C. D. S. Brites, P. P. Lima, N. J. O. Silva, A. Millán, V. S. Amaral, F. Palacio and L. D. Carlos, Thermometry at the nanoscale, *Nanoscale*, 2012, **4**, 4799–4829.

57 A. D. Becke, Density–functional thermochemistry. III. The role of exact exchange, *J. Chem. Phys.*, 1993, **98**, 5648–5652.

58 J. P. Perdew, M. Ernzerhof and K. Burke, Rationale for mixing exact exchange with density functional approximations, *J. Chem. Phys.*, 1996, **105**, 9982–9985.

59 D. Mester and M. Kállay, Charge-transfer excitations within density functional theory: how accurate are the most recommended approaches?, *J. Chem. Theory Comput.*, 2022, **18**, 1646–1662.

60 P.-F. Loos, M. Comin, X. Blase and D. Jacquemin, Reference energies for intramolecular charge-transfer excitations, *J. Chem. Theory Comput.*, 2021, **17**, 3666–3686.

61 T. Yanai, D. P. Tew and N. C. Handy, A new hybrid exchange–correlation functional using the Coulomb-attenuating method (CAM-B3LYP), *Chem. Phys. Lett.*, 2004, **393**, 51–57.

62 M. Casanova-Páez and L. Goerigk, Time-dependent long-range-corrected double-hybrid density functionals with spin-component and spin-opposite scaling: a comprehensive analysis of singlet-singlet and singlet-triplet excitation energies, *ChemRxiv*, 2021, DOI: **10.26434/chemrxiv.14706042**.

63 A. K. Dutta, F. Neese and R. Izsák, Towards a pair natural orbital coupled cluster method for excited states, *J. Chem. Phys.*, 2016, **145**, 034102.

64 A. K. Dutta, M. Nooijen, F. Neese and R. Izsák, Automatic active space selection for the similarity transformed equations of motion coupled cluster method, *J. Chem. Phys.*, 2017, **146**, 074103.

65 A. K. Dutta, M. Nooijen, F. Neese and R. Izsák, Exploring the accuracy of a low scaling similarity transformed equation of motion method for vertical excitation energies, *J. Chem. Theory Comput.*, 2017, **14**, 72–91.

66 M. Nooijen and R. J. Bartlett, Similarity transformed equation-of-motion coupled-cluster theory: details, examples, and comparisons, *J. Chem. Phys.*, 1997, **107**, 6812–6830.

67 M. Nooijen and R. J. Bartlett, A new method for excited states: similarity transformed equation-of-motion coupled-cluster theory, *J. Chem. Phys.*, 1997, **106**, 6441–6448.

68 J. Sous, P. Goel and M. Nooijen, Similarity transformed equation of motion coupled cluster theory revisited: a benchmark study of valence excited states, *Mol. Phys.*, 2013, **112**, 616–638.